



# Analysis of aging of commercial composite metal oxide – $\text{Li}_4\text{Ti}_5\text{O}_{12}$ battery cells



Pontus Svens <sup>a, b, \*</sup>, Rickard Eriksson <sup>c</sup>, Jörgen Hansson <sup>a</sup>, Mårten Behm <sup>b</sup>,  
Torbjörn Gustafsson <sup>c</sup>, Göran Lindbergh <sup>b</sup>

<sup>a</sup> Scania CV AB, SE-151 87 Södertälje, Sweden

<sup>b</sup> School of Chemical Science and Engineering, Department of Chemical Engineering and Technology, Applied Electrochemistry, KTH Royal Institute of Technology, SE-100 44 Stockholm, Sweden

<sup>c</sup> Department of Chemistry, Ångström Laboratory, Uppsala University, Box 538, SE-751 21 Uppsala, Sweden

## HIGHLIGHTS

- Changes in electrode balancing for commercial composite LMO–LCO/LTO battery cells due to cycling.
- We study material degradation of positive and negative electrodes for the examined cell type.
- The cell type was limited by loss of positive electrode capacity and by a virtual excess of cyclable lithium after cycling.
- Tested cell shows excellent calendar aging qualities with stable capacity and impedance over time.

## ARTICLE INFO

### Article history:

Received 18 April 2014

Received in revised form

4 July 2014

Accepted 9 July 2014

Available online 18 July 2014

### Keywords:

Hybrid electrical vehicle (HEV)

Lithium ion battery

$\text{Li}_4\text{Ti}_5\text{O}_{12}$

$\text{LiMn}_2\text{O}_4$

$\text{dV/dQ}$

$\text{dQ/dV}$

## ABSTRACT

Commercial battery cells with  $\text{Li}_4\text{Ti}_5\text{O}_{12}$  negative electrode and composite metal oxide positive electrode have been analyzed with respect to aging mechanisms. Electrochemical impedance spectroscopy (EIS), differential capacity analysis ( $\text{dQ/dV}$ ), differential voltage analysis ( $\text{dV/dQ}$ ) and scanning electron microscopy (SEM) with energy dispersive X-ray analysis (EDX) were used to identify different ageing mechanisms such as lithium inventory loss, loss of active electrode material and surface film growth. The active material of the positive electrode was also examined by X-ray diffraction (XRD). Aging mechanisms were studied for both calendar-aged and cycle-aged cells. Data from half cells prepared from post mortem harvested electrode material, using lithium foil as negative electrode and pouch material as encapsulation, were used as reference to full cell data. Electrochemical analysis of full and half cells combined with material analysis showed to be a powerful method to identify aging mechanisms in this type of commercial cells. The calendar-aged cell showed insignificant aging while the cycle-aged cell showed noticeable loss of positive electrode active material and loss of cyclable lithium, but only minor loss of negative electrode active material. The results imply that  $\text{Li}_4\text{Ti}_5\text{O}_{12}$  negative electrode material is a good alternative to other materials if high energy density is not the primary goal.

© 2014 Elsevier B.V. All rights reserved.

## 1. Introduction

The lifetime of a lithium-ion battery is one of several challenging factors that need to be addressed when used in a hybrid electric vehicle (HEV) application. The requirements on HEV batteries differ significantly from requirements on for example batteries intended

for consumer electronics products. Hence, battery cell manufacturers need to develop specific batteries for automotive applications. It is for example desirable to be able to use HEV batteries at elevated temperatures to avoid large and expensive battery cooling systems. To maximize battery life it is also essential to adapt the usage of a battery according to its state of health. For example, optimization of usage of available energy and power in an HEV battery is every moment based on the battery state of charge, SOC, which is correlated to the open circuit voltage, OCV. The relationship between OCV and SOC changes when a battery is aged depending on usage and could cause errors in the SOC-estimation

\* Corresponding author. Scania CV AB, SE-151 87 Södertälje, Sweden. Tel.: +46 8 553 51661; fax: +46 8 553 82841.

E-mail addresses: [pontus.svens@scania.com](mailto:pontus.svens@scania.com), [ponsvens@kth.se](mailto:ponsvens@kth.se) (P. Svens).



in an HEV battery if not accounted for. Another issue that needs to be addressed is the voltage limits of the battery cell. Initial electrode matching during production of a battery cell assures individual electrode potentials to stay within a defined stable electrochemical window if the cell voltage always is kept within the specified limits. When a cell is aged the initial electrode matching changes and this could cause individual electrode potentials to get out of the stable electrochemical window even if the cell voltage is kept within limits, thus causing accelerated aging. It is hence important for automotive companies to have a more detailed understanding about how aging influences different cell parameters throughout the lifetime of a battery to be able to optimize battery usage and maximize lifetime. Previous studies of commercial cells by for instance Bloom et al. [1–3] and Smith et al. [4,5] have proven that the methods incremental capacity ( $dQ/dV$ ) and differential voltage analysis ( $dV/dQ$ ) are useful for revealing detailed information about aging mechanisms when applied on both full cell data and corresponding half cell data. However, studies of this type have previously focused on commercial cells using graphite as negative electrode active material which not is optimal for the high charge power demands of batteries for heavy-duty vehicles. In the previous studies the negative electrode has been reported to be the main contributor to aging, in combination with loss of active lithium inventory. Lithium titanate,  $\text{Li}_4\text{Ti}_5\text{O}_{12}$ , is a negative electrode active material that meets the demands for high power battery charging in HEV's and a high cycle life would also be expected from this material due to the zero-strain characteristics.  $\text{Li}_4\text{Ti}_5\text{O}_{12}$  intercalates to  $\text{Li}_7\text{Ti}_5\text{O}_{12}$  while changing structure from spinel to rock-salt-type with an insignificant volume change [6,7]. This zero-strain nature also makes it possible to utilize a large SOC-window without sacrificing lifetime of the negative electrode. One growing market for battery cells using lithium titanate negative electrodes is mild hybrid passenger cars. There are today commercial battery modules available intended for use in passenger cars to optimize the idle stop-start functionality [8,9]. There are several material studies on  $\text{Li}_4\text{Ti}_5\text{O}_{12}$  available in the literature [7,10,11] but there is a lack of studies regarding aging of commercial cells of this type.

This study aims to investigate aging of commercial composite metal oxide/ $\text{Li}_4\text{Ti}_5\text{O}_{12}$  cells with advanced electrochemical methods using standard battery cycling equipment with impedance measurement option and with material analysis methods. The methods incremental capacity analysis ( $dQ/dV$ ), differential voltage analysis ( $dV/dQ$ ), electrochemical impedance spectroscopy (EIS), scanning electron microscopy (SEM) with energy dispersive X-ray spectroscopy (EDX), and X-ray diffraction (XRD) were used in this study.

## 2. Experimental

Commercial prismatic composite metal oxide/ $\text{Li}_4\text{Ti}_5\text{O}_{12}$  cells with a rated initial capacity of 3.1 Ah and a nominal voltage of 2.4 V were acquired from a reputable supplier for this study. The positive electrode composite metal oxide material consisted of  $\text{LiCoO}_2$  and  $\text{LiMn}_2\text{O}_4$ . The cell type was prismatic with dimensions  $62 \times 13 \times 96$  mm ( $W \times D \times H$ ). Cycling was performed on in-house developed equipment primarily intended for battery cycling on-board vehicles [12,13]. Two cells were used in this study. Both cells were stored for 13 months at 23 °C at 50% SOC prior to the test. After the initial storage period one cell was cycled galvanostatically, while the other cell was kept under storage conditions during the same time. The cycled cell was continuously charged and discharged with a constant current (6.8 A) between upper and lower voltage limits specified by the supplier (2.8 V and 1.5 V respectively). Cycling was performed at 55 °C and the total testing time was 9 months, corresponding to 9201 full cycles. Thereafter the cells were stored again at room temperature for 30 months. Finally

the performance of the cells was investigated with electrochemical methods, followed by disassembling the cells and harvesting electrode samples. Samples were taken from the middle part of the width of the jellyroll, approximately 40 cm from the outer end of the unwound roll. The total length of the unwound roll was 390 cm. Both cells originated from the same batch and the time between cell production and electrode material harvesting was approximately 55 months. The performance of the cycle-aged cell was periodically measured during the test. Capacity measurements (3.6 A and 25 °C) were performed on the in-house developed battery cycling equipment and impedance measurements (10 mV voltage amplitude and 25 °C) on a Solartron SI 1260 Impedance/Gain-phase analyzer.

After final capacity and impedance measurements the cells were opened in an argon filled glove box (<1 ppm  $\text{H}_2\text{O}$ ). The calendar-aged cell was opened at SOC ~0% and the cycle-aged cell at SOC ~50%. Samples were harvested by cutting out circular pieces of  $9.6 \text{ cm}^2$  from both electrodes. One side of each electrode was cleaned from active material using N-methyl-2-pyrrolidone (NMP) (Merck). Care was taken to prevent any NMP to touch the other side of the electrode during the procedure. The samples were rinsed in dimethyl carbonate (DMC) (SelectiLyte, Merck) and left to dry for 30 min before being assembled to cells or vacuum-packed for SEM analysis. Half cells were made from the positive and negative electrodes respectively using lithium foil as combined reference and counter electrode (two electrode cell), a glass microfiber filter separator (Whatman GF/A) and nickel and aluminum current collectors. The electrolyte used was 1 M  $\text{LiPF}_6$  in EC/DEC (1:1 by weight, Merck LP40). The half cells were encapsulated in pouch material (polymer coated aluminum laminate) and vacuum sealed inside the glove box.

Charge and discharge measurements performed at 25 °C prior to opening the cells and on half cells were carried out using a Solartron SI 1287 electrochemical interface. The calendar-aged cell was measured at  $\pm 170$  mA (~C/20 rate) and the cycle-aged cell at  $\pm 27$  mA (~C/100 rate). The C-rates are based on actual cell capacity at that point in time, where 1 C is the current needed for discharging a cell in 1 h. Measurements on the half cell with calendar-aged positive electrode material were performed at  $\pm 0.16$  mA (~C/40 rate) and measurements on the half cell with calendar-aged negative electrode material were performed at  $\pm 0.056$  mA (~C/100 rate). Measurements on the half cell with cycle-aged positive electrode material were performed at  $\pm 0.042$  mA (~C/100 rate) and measurements on the half cell with cycle-aged negative electrode material were performed at  $\pm 0.048$  mA (~C/100 rate). The use of very small currents assured negligible impact of polarization resistance on the voltage profiles. Electrochemical impedance spectroscopy (EIS) was performed on a Solartron SI 1260 Impedance/Gain-phase analyzer. The full cell measurements were performed with voltage amplitude of 10 mV and the half cell measurements with voltage amplitude of 0.5 mV.

All collected samples were rinsed in DMC and kept under argon atmosphere before performing SEM/EDX/XRD analysis. The SEM/EDX-samples were mounted onto sample holders and exposed to air for less than 5 min before analysis. The electrode material needed for XRD measurements were extracted from electrode samples by gently peeling off the current collectors after attaching it to Kapton<sup>®</sup> tape, leaving the electrode material on a low background Kapton tape suitable for transmission X-ray diffraction. The tape-samples were mounted in sample holders with a 5 mm opening and all samples were measured in air.

SEM-imaging were performed on a Zeiss Sigma VP using an acceleration voltage of 5 kV and a vacuum of  $<10^{-8}$  bar. Energy dispersive X-ray (EDX) detection was performed at 20 kV using an Oxford instruments X-max 50 detector.



X-ray diffraction measurements (XRD) were performed on an STOE diffractometer with a Mythen 1 K Silicon-strip solid-state detector using  $\text{CuK}\alpha_1$  radiation. Diffraction patterns were collected for  $2\theta$ -angles between  $10^\circ$  and  $94^\circ$  and Rietveld refinements were done with FullProf-software [14] using a Pseudo-Voigt profile function. Starting models for the materials were  $\text{LiMn}_2\text{O}_4$  (space group  $Fd-3m$ ,  $a = 8.2211\text{\AA}$ ) [15] and  $\text{LiCoO}_2$  (space group  $R-3m$ ,  $a = 2.8265\text{\AA}$ ,  $c = 13.89\text{\AA}$ ) with no lithium–cobalt mixing [16]. For each phase the following parameters were refined: scale factor, cell parameters and peak width parameters (standard UFW function). For the  $\text{LiCoO}_2$  phase a preferred orientation function was used to compensate for an assumed (001)-direction plate-like microstructure in the material. Additional parameters for the two samples were polynomial background (6 parameters) and zero point. Peak asymmetry due to geometry of the test setup was handled by two parameters refined dependently for all measurements and all peaks below  $62^\circ$  were corrected regarding asymmetry.

### 3. Results and discussion

#### 3.1. Capacity measurements

The capacity of the cycled cell was measured periodically during the test period. Cycling was ended at cycle 9201, corresponding to 71 kWh energy throughput or approximately 30,000 Ah. Fig. 1a shows discharge curves for the cycled cell at different cycle numbers, when discharged with 3.6 A ( $\sim 1$  C rate initially). Fig. 1b shows discharge curves for both cycled-aged and calendar-aged cells at the beginning of testing and prior to cell opening. It is seen that the cycle-aged cell capacity measured at 3.6 A prior to opening the cell (Fig. 1a) is significantly lower than the measured C/40 capacity (Fig. 1b), indicating high cell impedance. It is also seen from Fig. 1a that there is a significant difference between the capacity at the end of testing and the capacity measured just before opening the cell. This difference in capacity could be a result of calendar aging since the cell was stored at  $\sim 25^\circ\text{C}$  for several

months between end of test and the last measurement before cell opening. The capacity loss between the last cycle and prior to cell opening indicates a faster calendar aging process during this time period compared to the calendar-aged cell, suggesting that calendar aging mechanisms are connected to the history of usage in this specific case. The cycle-aged cell had at the end of test lost 29% of the starting capacity while the calendar-aged cell had retained its capacity during the test period, indicating negligible capacity loss due to calendar aging at room temperature for this type of cell.

When opening the cells, it was observed that the can of the cycle-aged cell was noticeably more swollen than the can of the calendar-aged cell. Moreover, there was no free electrolyte in the can of the cycle-aged cell, but free electrolyte was observed in the can of the calendar-aged cell. This implies that electrolyte has been consumed in gas producing reactions, possibly causing loss of cyclable lithium in the cycle-aged cell. This assumption was supported by visual inspection of the two jellyrolls after cell opening. No difference in size was observed when comparing the calendar-aged jellyroll with the cycle-aged one. Half cell capacities of harvested electrode material samples are presented in Fig. 1c and d. Fig. 1c displays voltage profiles for the positive electrode material showing a 27% lower discharge capacity for the cycle-aged sample than for the calendar-aged sample. Voltage profiles of the negative electrode material are presented in Fig. 1d, and are only showing about 5% difference in discharge capacity between the cycle-aged sample and calendar-aged sample. The initial electrode capacities are assumed to be close to that of the calendar-aged cell. This assumption is based on half cell measurements on samples from a fresh cell from a different batch with a slightly changed cell chemistry (not presented here). The fresh half cell capacities showed similar results as calendar-aged half cell capacities; hence it is assumed that both the positive and the negative electrode capacity has been retained for the calendar-aged cell. We have in an earlier study showed that aging can be spatially distributed across the jellyroll [45]. This uneven electrode aging was found to be correlated to variations in appearance along the jellyroll, visible for

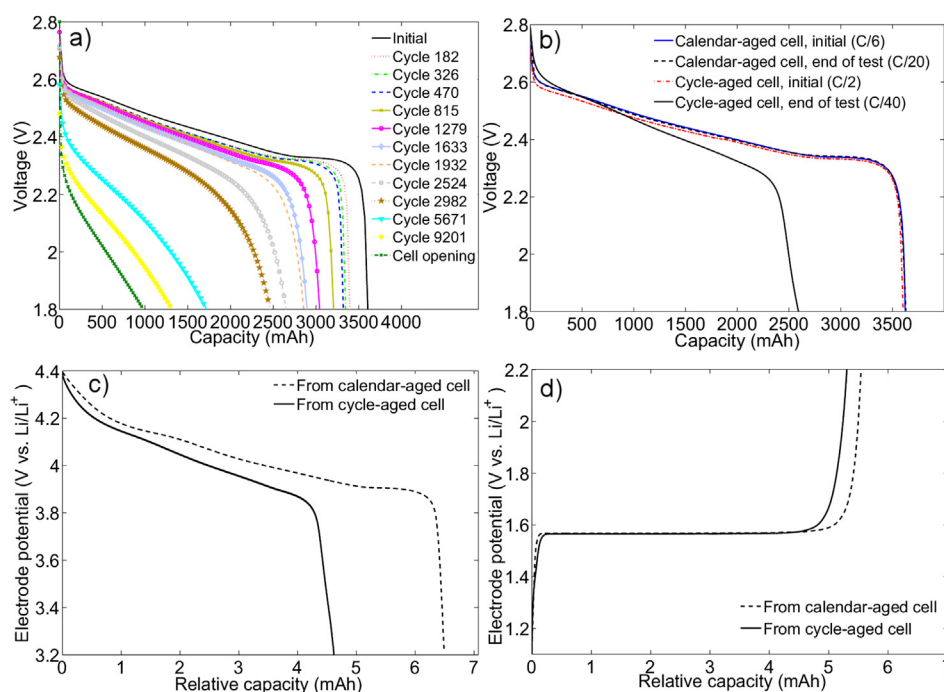


**Fig. 1.** (a) Discharge capacity at 3.6 A and  $25^\circ\text{C}$  for the cycle-aged cell, (b) initial calendar-aged cell capacity and cycle-aged cell capacity and capacities at end of test, (c) calendar-aged and cycle-aged positive electrode capacity (C/40 and C/100), (d) calendar-aged and cycle-aged negative electrode capacity (C/40 and C/100).



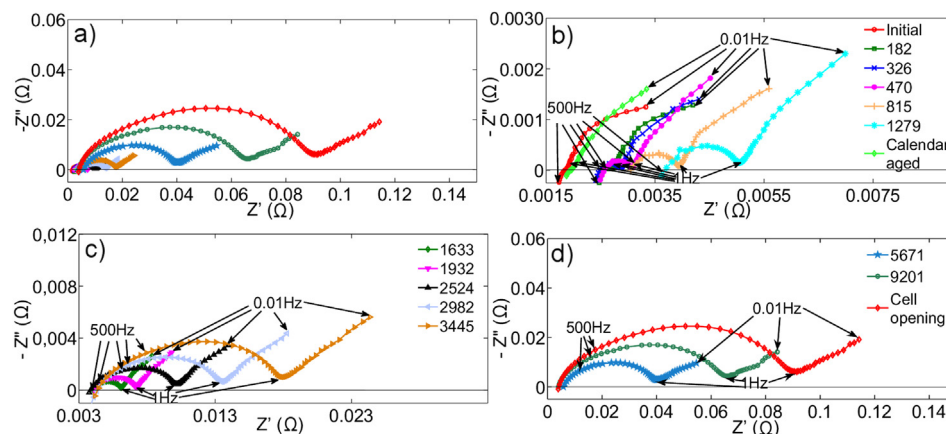


**Fig. 2.** (a) Nyquist plots for both cycle-aged and calendar-aged cells measured at SOC 50% and 25 °C (b) Nyquist plots with data from initial performance to cycle 1279, including calendar-aged cell. (c) Nyquist plots with data from cycle 1633 to 3445. (d) Nyquist plots with data from cycle 5671 to end of test.

the naked eye. In this paper we chose to only harvest samples from one position for each electrode and cell since no obvious difference in appearance along the jellyroll was seen in this case.

### 3.2. Electrochemical impedance spectroscopy

To find the main source for the observed impedance rise of the cycle-aged cell, EIS was performed on both full cell and half cell samples. Fig. 2 shows impedance (Nyquist) plots over both the cycle-aged cell and the calendar-aged cell. Fig. 2 shows an overview of Nyquist plots for different cycle numbers. Since there is a big difference in impedance between the measurements at the beginning of the test and at the end of the test, the Nyquist plots are divided into three separate plots presented in Fig. 2b–d for better visibility. The calendar-aged cell impedance is also presented in Fig. 2b, showing only a minor difference in impedance from the initial value. It is noticeable from Fig. 2b that the semicircle in the frequency region ~500 Hz–1 Hz is extremely small when the cells are fresh, indicating very fast charge transfer kinetics. During aging, the most visible change is a significant growth of the semicircle.

Fig. 3a shows Nyquist plots for both cycle-aged and calendar-aged half cell samples of both electrodes and Fig. 3b shows a zoomed in picture of Fig. 3a. The cycle-aged positive electrode sample has an extremely large semicircle (~500 kHz–0.1 Hz) compared to the calendar-aged electrode sample, signifying that the positive electrode is the main impedance contributor for the cycle-aged cell. It is also seen that the difference in negative electrode impedance between the calendar-aged half cell sample and the cycle-aged half cell sample is fairly small, emphasizing that the impedance rise of the cycle-aged cell is mainly related to the positive electrode. Studies of commercial battery cells containing LiCoO<sub>2</sub> and LiMn<sub>2</sub>O<sub>4</sub> positive electrode material have earlier reported similar large growth of semicircles for aged positive

electrode material, with increased interfacial impedance as one of several proposed root causes [17–19].

### 3.3. Scanning electron microscopy

SEM-imaging was done to study the appearance and morphology of harvested electrode material. Micrographs for both positive and negative electrode materials are presented in Fig. 4. All samples were collected from the center of the electrode jellyrolls and at a position approximately 20 cm from the outer end of the unwound jellyroll. Micrographs of the positive electrode sample are shown in Fig. 4a and b, and micrographs of the negative electrode sample are shown in Fig. 4c and d. No obvious difference between cycle-aged and calendar-aged materials could be seen for either the positive or the negative electrode, indicating only minor solid electrolyte interphase (SEI) build up on both electrodes. However, since SEM has a certain image depth profile depending on the penetration depth of the electron beam into the analyzed material, more surface specific analysis methods would be required to confirm this statement. This result could however be expected for the negative electrode since Li<sub>4</sub>Ti<sub>5</sub>O<sub>12</sub> has a high electrode potential vs. lithium (1.55 V) which is within the electrochemically stable potential window for the electrolyte, hence reducing growth of SEI.

Presence of both Mn and Co in the positive electrode material was confirmed using EDX. The EDX-mapping pictures in Fig. 5a and b displays Co-containing areas as green and Mn-containing areas as purple. The findings indicate presence of both LiMn<sub>2</sub>O<sub>4</sub> and LiCoO<sub>2</sub> in the positive electrode material. Lithium metal oxides, most often transition-metal oxides, are commonly used as positive electrode material mainly due to high potential vs. Li/Li<sup>+</sup> and high specific capacity. Park et al. and Kosova et al. suggest that LiCoO<sub>2</sub> together with LiMn<sub>2</sub>O<sub>4</sub> improves the rate capability of the composite positive electrode material [20,21]. Both materials have a high nominal

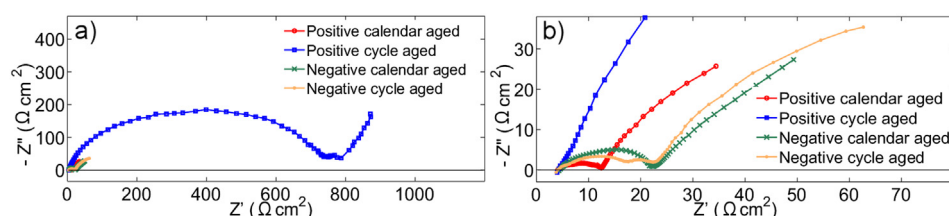


**Fig. 3.** (a) Impedance for positive and negative electrode half cell samples (b) zoomed in picture.



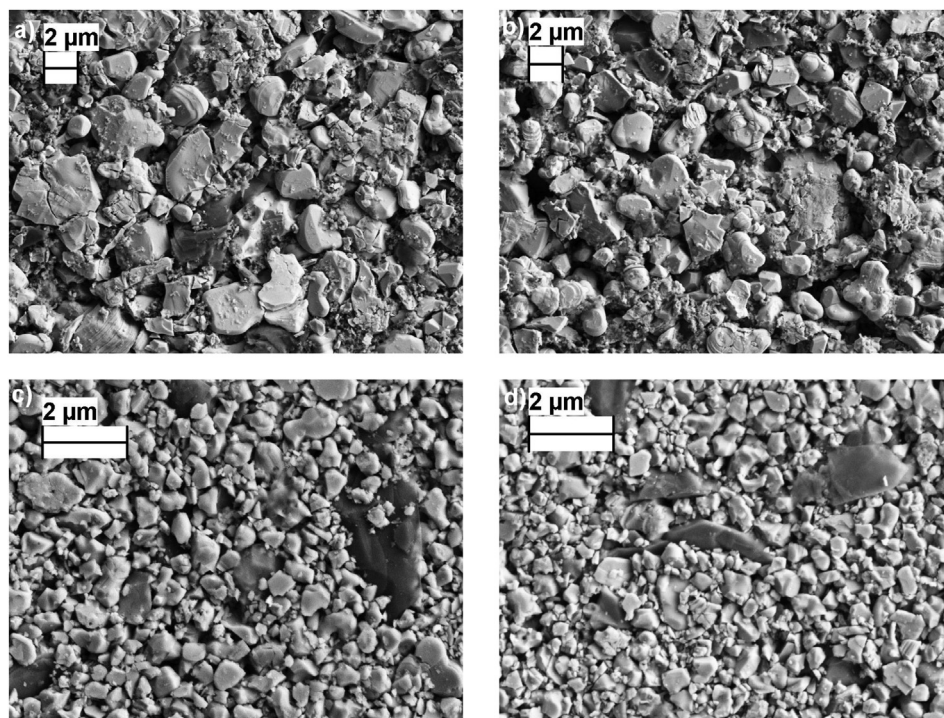


**Fig. 4.** SEM-images (a) calendar-aged  $\text{LiMn}_2\text{O}_4/\text{LiCoO}_2$  at 10 k magnification. (b) Cycle-aged  $\text{LiMn}_2\text{O}_4/\text{LiCoO}_2$  at 10 k magnification. (c) Calendar-aged  $\text{Li}_4\text{Ti}_5\text{O}_{12}$ , at 25 k magnification. (d) Cycle-aged  $\text{Li}_4\text{Ti}_5\text{O}_{12}$  at 25 k magnification.

potential vs. lithium ( $\sim 4$  V) and together with  $\text{Li}_4\text{Ti}_5\text{O}_{12}$  negative electrode material a nominal cell voltage of  $\sim 2.5$  V is provided. Fig. 5a shows a calendar-aged positive electrode sample and Fig. 5b a cycle-aged electrode sample. The interfaces between particles for

the cycle-aged material in Fig. 5b seems to be more diffuse than the interfaces between particles for the calendar-aged material in Fig. 5a. This effect was seen all over the analyzed sample, but was not measured on different locations of the jellyroll. This indicates

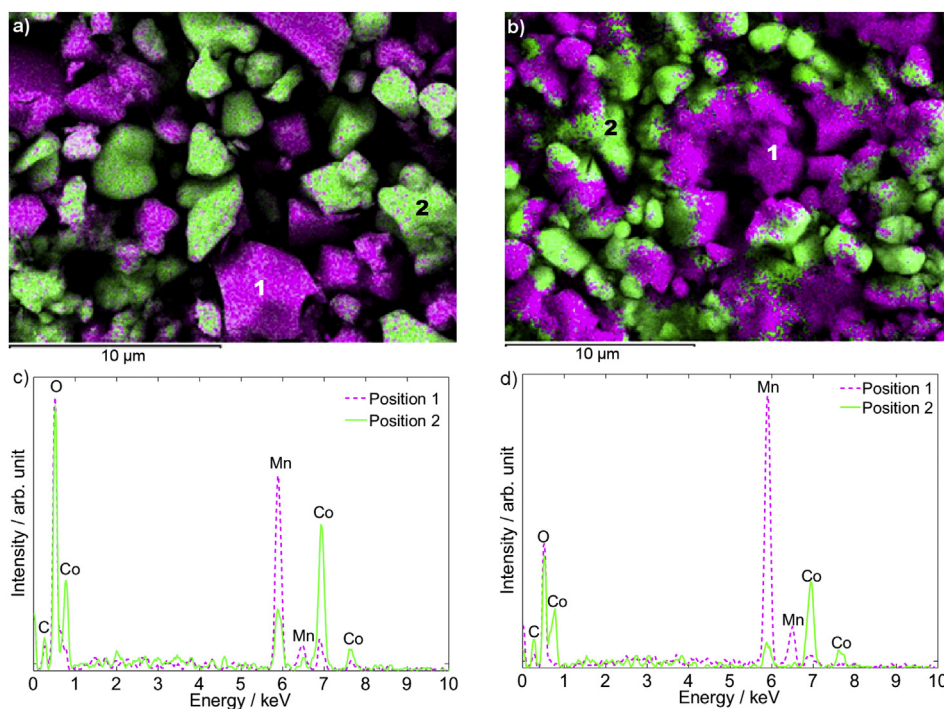


**Fig. 5.** EDX-mapping pictures from (a) calendar-aged positive sample and (b) cycle-aged positive sample. Green color represents the cobalt signal, magenta color represents the manganese signal. (c) Point-EDX plot from position 1 and 2 in Fig. 5a. (d) Point-EDX plot from position 1 and 2 in Fig. 5b. (For interpretation of the references to color in this figure legend, the reader is referred to the web version of this article.)



that transportation of material between  $\text{LiMn}_2\text{O}_4$  and  $\text{LiCoO}_2$  has occurred during cycling.

Fig. 5c and d presents point-EDX plots from the specified positions 1 and 2 in Fig. 5a and b. The point-EDX curves gives information about the relationship between the manganese signal and the cobalt signal for the different colored areas in Fig. 5a and b. In addition, it is observed that the relationship between the manganese signal and the oxygen signal is significantly higher for the cycle-aged cell sample compared to the calendar-aged cell sample. This behavior is not seen for the relationship between the cobalt and the oxygen signal, indicating that the  $\text{LiMn}_2\text{O}_4$  phase is more affected by cycling than the  $\text{LiCoO}_2$  phase. EDX-measurements were also done on both calendar-aged and cycle-aged negative electrode samples (Fig. 6). The inset picture in Fig. 6 shows that manganese is present in the cycled-aged negative electrode but not in the calendar-aged one. This could possible contribute to the small loss of capacity seen for the negative electrode. This also supports the findings from the positive electrode samples and strengthens the theory that the  $\text{LiMn}_2\text{O}_4$  phase has been more affected by cycling than the  $\text{LiCoO}_2$  phase.

### 3.4. X-ray diffraction measurements

The presence of both  $\text{LiMn}_2\text{O}_4$  and  $\text{LiCoO}_2$  in the positive electrode material was also identified by XRD. No significant difference in composition between the cycle-aged and the calendar-aged sample was found, both samples showed a weight fraction of ~50% for each phase, which is in line with the EDX findings. Small changes in cell parameters were found as expected from samples with different SOC [22,23]. The most significant results from XRD measurements were broadening of Bragg peaks (calculated as  $\text{FWHM} = \sqrt{(U \tan^2(\theta) + V \tan(\theta) + W)}$ ). An increased peak width was found for both phases in the cycle-aged sample compared to the calendar-aged sample (Fig. 7). A broadening of peaks can be seen in the zoomed in pictures in Fig. 7b and c, especially for the  $\text{LiMn}_2\text{O}_4$  phase. These results indicate that the crystallinity of the  $\text{LiMn}_2\text{O}_4$  phase to some extent has been affected more than the  $\text{LiCoO}_2$  phase by cycling, which is in line with the EDX findings.

### 3.5. Incremental capacity analysis

Incremental capacity analysis (dQ/dV) is a method that identifies areas in the voltage profile correlated to phase equilibrium of active

electrode material, manifested as flat regions in the voltage profile. Full cell dQ/dV analysis has earlier been performed by several research groups. Smith et al. have performed dQ/dV analysis on aged cells containing  $\text{LiMn}_2\text{O}_4$ /graphite and  $\text{LiCoO}_2$ /graphite including analysis of corresponding half cells [5,24]. Dubarry et al. have performed cycle aging of cells containing  $\text{LiFePO}_4$ /graphite and used dQ/dV to identify aging mechanisms [25,26]. Changes in the dQ/dV curves can help to identify aging mechanisms in a battery cell. This method has also been investigated for usage in electrified vehicles to estimate state of health (SOH) of a battery pack [27,28].

Fig. 8a shows full cell dQ/dV of both charge and discharge data from both cycle-aged and calendar-aged cells. The plots reveal a distinctive peak at ~2.35 V and two diffuse peaks at ~2.45 V and ~2.6 V respectively (marked with arrows in Fig. 8a). Since  $\text{LiMn}_2\text{O}_4$  only has two peaks according to literature, the existence of a third peak should relate to the presence of  $\text{LiCoO}_2$  [20,29–33]. The peaks in Fig. 8a should only belong to the positive electrode material since the negative electrode consists of a two phase material with only one very broad voltage plateau. Fig. 8b shows dQ/dV-plots for the cycled cell at different currents and it is observed that even a C/40-current rate is too high to be able to clearly identify all peaks. Reducing the current rate to C/100 makes it possible to identify three peaks (marked with arrows in Fig. 8b) corresponding to the peaks observed for the calendar-aged cell. In addition, it is clear that there are only small differences in voltage for charge and discharge peaks respectively indicating that the polarization is small at this current. A broadening of the  $\text{LiMn}_2\text{O}_4$  peaks and the  $\text{LiCoO}_2$  peak is seen when comparing the plot for the cycle-aged cell with the plot for the calendar-aged cell (Fig. 8a), indicating slower electrode kinetics for both the  $\text{LiMn}_2\text{O}_4$  phase and the  $\text{LiCoO}_2$  phase in the cycle-aged cell [34]. Fig. 8c shows dQ/dV-plots for half cells with positive electrode samples. The plots show peaks at ~3.9 V vs.  $\text{Li/Li}^+$ , verifying presence of  $\text{LiCoO}_2$  [20,29] in accordance with the findings from SEM-EDX and XRD. The additional peaks at ~4.0 V and ~4.15 V confirms presence of  $\text{LiMn}_2\text{O}_4$  [30]. A broadening of the  $\text{LiCoO}_2$  peak and the  $\text{LiMn}_2\text{O}_4$  peaks is also seen here. The atomic structure of  $\text{LiMn}_2\text{O}_4$  is of spinel type and during lithiation a transformation from  $\text{Mn}_2\text{O}_4$  to  $\text{LiMn}_2\text{O}_4$  takes place in two steps [33]. The layered transition metal oxide material  $\text{LiCoO}_2$  changes stoichiometry from  $\text{LiCoO}_2$  to  $\text{Li}_{0.5}\text{CoO}_2$  during charging and that is the lowest delithiation degree for a reversible electrochemical reaction for this material. The observed broadening of dQ/dV-peaks for both  $\text{LiMn}_2\text{O}_4$  and  $\text{LiCoO}_2$  could relate to metal ion transportation between  $\text{LiMn}_2\text{O}_4$  and  $\text{LiCoO}_2$ . For example has substitution of manganese for cobalt in the lithium manganese spinel structure previously been reported in literature [21,35]. This is in line with the EDX-findings where metal ion substitution could explain the more diffuse interfaces between particles in the cycle-aged sample. It is also reported in literature that heavily cycled layered  $\text{LiCoO}_2$  electrode active material can transform into a more inert cubic spinel form,  $\text{Li}_2\text{Co}_2\text{O}_4$ , causing irreversible capacity loss [36–38], but this phase was in this study not detected by XRD. However, in the previous studies TEM measurements were used to observe existence of the spinel  $\text{Li}_2\text{Co}_2\text{O}_4$  phase and that method is capable of detecting much smaller domains of crystalline materials compared to XRD. Presence of  $\text{Li}_2\text{Co}_2\text{O}_4$  could be one possible explanation to the increased impedance seen for the cycle-aged cell since  $\text{Li}_2\text{Co}_2\text{O}_4$  has lower conductivity than  $\text{LiCoO}_2$ . Another possible mechanism that could cause loss of positive electrode active material is  $\text{Mn}^{2+}$  dissolution. There are several reports in the literature describing  $\text{Mn}^{2+}$  dissolution, especially at elevated temperatures [39–41]. The proposed aging mechanism is formation of  $\text{Mn}^{3+}$  due to acid dissolution of the spinel structure. The acidic environment is reported to relate to HF formed by decomposition

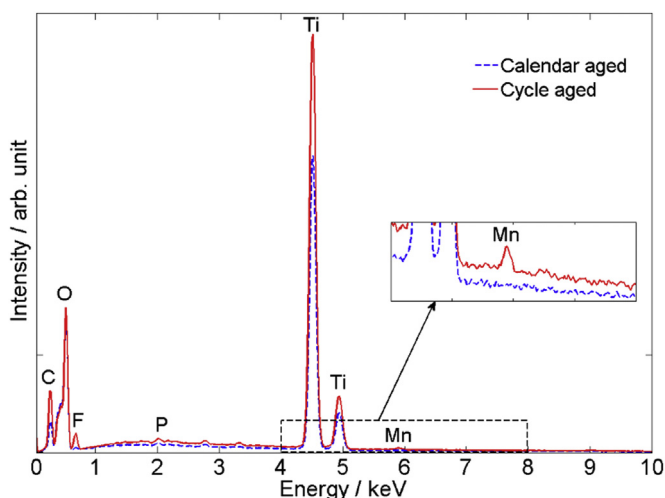
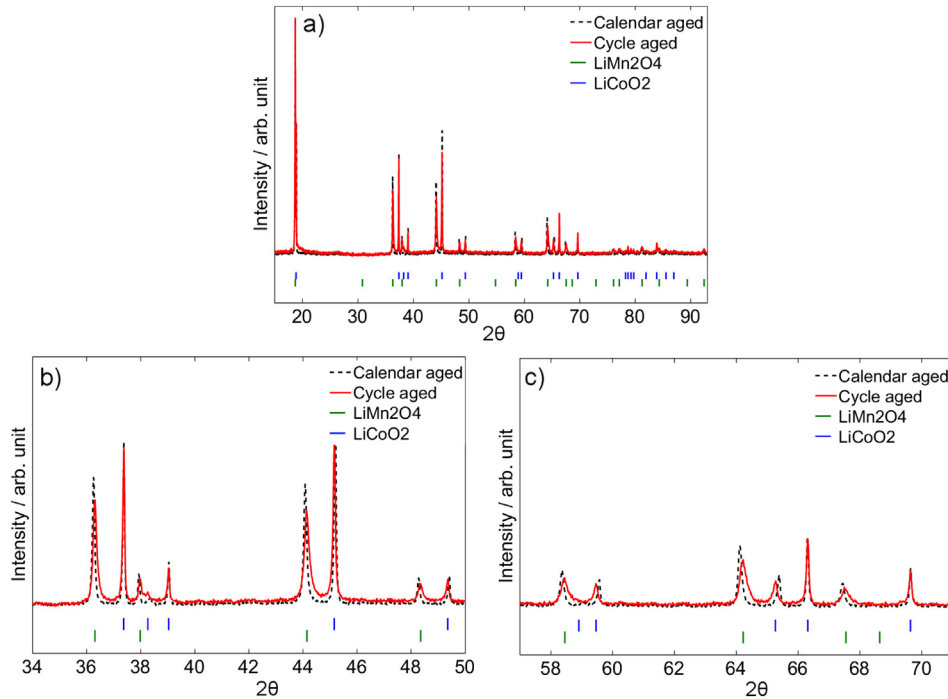


Fig. 6. Point-EDX plots from calendar-aged and cycle-aged negative electrode samples.





**Fig. 7.** X-ray diffraction patterns for calendar-aged and cycle-aged positive electrode material. (a) Calculated diffraction pattern for the mixed positive electrode material over a  $2\theta$ -span from 15 to 95. (b) Zoomed in picture over a  $2\theta$ -span from 34 to 50. (c) Zoomed in picture over a  $2\theta$ -span from 57 to 71.

of the lithium salt,  $\text{LiPF}_6$ . The  $\text{Mn}^{3+}$  ions is reacting further forming  $\text{Mn}^{4+}$  and  $\text{Mn}^{2+}$ , of which  $\text{Mn}^{2+}$  is dissolved in the electrolyte. This is in line with both EDX-findings and XRD-findings.

Fig. 8d shows  $dQ/dV$  vs. potential plots for half cells consisting of harvested negative electrode material. The only and distinct peak at  $\sim 1.55$  V vs.  $\text{Li/Li}^+$  clearly confirms the presence of  $\text{Li}_4\text{Ti}_5\text{O}_{12}$  [10,11]. This peak is broader and lower for the cycle-aged cell than for the calendar-aged cell indicating slower electrode kinetics [10]. According to literature, this could relate to surface reactions between  $\text{Li}_4\text{Ti}_5\text{O}_{12}$  and the electrolyte solvent, forming a thin surface film [42]. Formation of a surface film on  $\text{Li}_4\text{Ti}_5\text{O}_{12}$  is reported to occur foremost during cycling by consumption of solvent while forming gas consisting mainly of  $\text{CO}_2$ ,  $\text{H}_2$  and  $\text{CO}$ . This is in line with the observation of the swollen can of the cycled cell and the lack of free electrolyte.

### 3.6. Differential voltage analysis

The  $dQ/dV$ -method is not suitable for fitting half cell data to full cell data since half cell  $dQ/dV$ -data cannot be added together to obtain  $dQ/dV$ -data for a full cell [1]. In this case, it is more suitable to use differential voltage analysis,  $dV/dQ$ . The derivation of equations needed for this fitting process has earlier been presented in literature [25,26,43,44]. A summary of those derivations is presented here.

The open circuit voltage, OCV, is the difference between the positive and the negative electrode potential, as illustrated by Equation (1).

$$V_{\text{cell}}(Q_{\text{cell}}) = V_{\text{pos}}(Q_{\text{cell}}) - V_{\text{neg}}(Q_{\text{cell}}) \quad (1)$$

In a perfectly matched battery the full cell capacity is equal to both the negative and the positive electrode capacity, according to Fig. 9.

In this particular case, the full cell voltage,  $V_{\text{cell}}$ , the positive electrode potential,  $V_{\text{pos}}$ , and the negative electrode potential,  $V_{\text{neg}}$ ,

is all a function of the present charge of the full cell,  $Q_{\text{cell}}$ . This means that in a perfectly matched cell, both the desired lower cut-off potential for the positive electrode and the desired higher cut-off potential for the negative electrode coincides with the lower cut-off voltage for the full cell at fully discharged state (Fig. 9). The analogous reasoning is valid at the fully charged state. However, even in a battery cell with matched electrodes in terms of capacity, the useful cell capacity is often lower than the individual electrode capacities since the fully discharged state of the individual electrodes might not coincide with the fully discharged state of the cell. This is described as a shift of the OCV curve along the x-axis for each electrode relative the full cell OCV, as described by Equations (2) and (3) below:

$$Q_{\text{pos}} = Q_{\text{cell}} - \delta_{\text{pos}} \quad (2)$$

$$Q_{\text{neg}} = Q_{\text{cell}} - \delta_{\text{neg}} \quad (3)$$

The shift is called slippage and is denoted  $\delta$  [mAh]. By including Equations (2) and (3) into Equation (1) the following expression is obtained:

$$V_{\text{cell}}(Q_{\text{cell}}) = V_{\text{pos}}(Q_{\text{pos}} + \delta_{\text{pos}}) - V_{\text{neg}}(Q_{\text{neg}} + \delta_{\text{neg}}) \quad (4)$$

Measurements are performed on half cells to obtain OCV curves for each electrode and the half cell capacity needs to be scaled to fit the full cell positive and negative electrode capacities respectively, according to Equations (5) and (6):

$$Q_{\text{pos}} = s_{\text{pos}} q_{\text{pos}} \quad (5)$$

$$Q_{\text{neg}} = s_{\text{neg}} q_{\text{neg}} \quad (6)$$

The scaling factor is denoted  $s$  [unit less] and the capacity for each half cell electrode sample is denoted  $q$  [mAh]. If the specific electrode capacity is known, the scaling factor will be equal to the



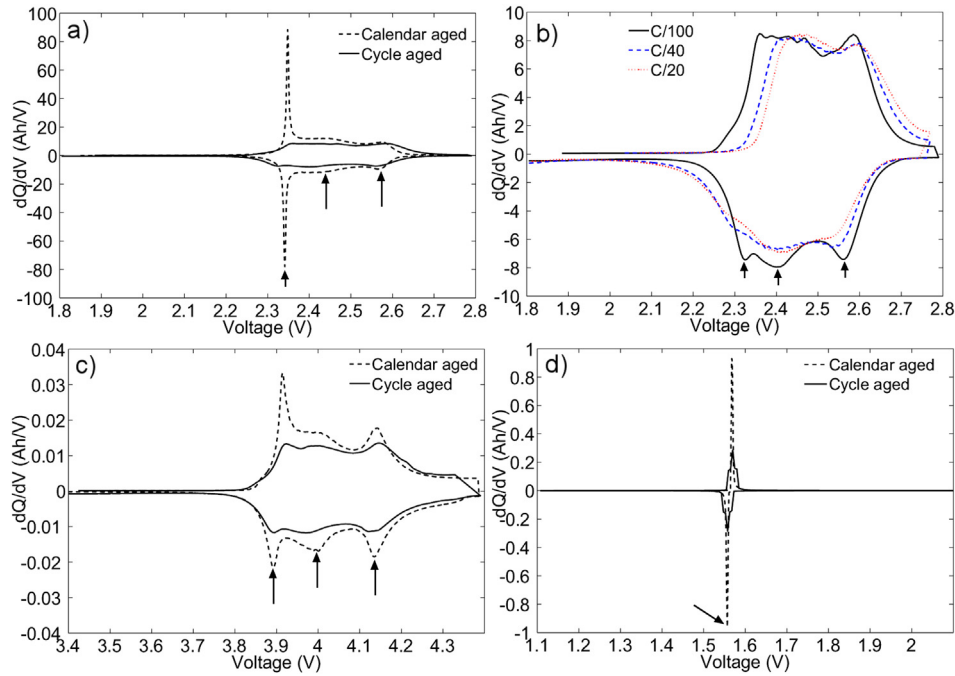


**Fig. 8.** dQ/dV-plots measured prior to cell opening for (a) calendar-aged cell (C/20) and cycle-aged cell (C/100), (b) cycle-aged cell at different currents, (c) positive electrode vs. lithium (C/100), (d) negative electrode vs. lithium (C/100).

mass of the active material. Combining Equation (4) with Equations (5) and (6) gives an expression for calculating the full cell OCV from half cell data:

$$V_{\text{cell}}(Q_{\text{cell}}) = V_{\text{pos}}(s_{\text{pos}}q_{\text{pos}} + \delta_{\text{pos}}) - V_{\text{neg}}(s_{\text{neg}}q_{\text{neg}} + \delta_{\text{neg}}) \quad (7)$$

However, all of the unknown parameters above cannot be found solely from Equation (7). An additional equation is hence needed and is obtained by differentiating Equation (7) with respect to the capacity:

$$\frac{dV_{\text{cell}}}{dQ_{\text{cell}}} = \frac{dV_{\text{pos}}(s_{\text{pos}}q_{\text{pos}} + \delta_{\text{pos}})}{dQ_{\text{pos}}} - \frac{dV_{\text{neg}}(s_{\text{neg}}q_{\text{neg}} + \delta_{\text{neg}})}{dQ_{\text{neg}}} \quad (8)$$

By combining Equations (5), (6) and (8) the following expression is obtained:

$$\frac{dV_{\text{cell}}}{dQ_{\text{cell}}} = \frac{dV_{\text{pos}}(s_{\text{pos}}q_{\text{pos}} + \delta_{\text{pos}})}{d(s_{\text{pos}}q_{\text{pos}})} - \frac{dV_{\text{neg}}(s_{\text{neg}}q_{\text{neg}} + \delta_{\text{neg}})}{d(s_{\text{neg}}q_{\text{neg}})} \quad (9)$$

Since  $s_{\text{pos}}$  and  $s_{\text{neg}}$  are constants, Equation (9) can finally be rewritten as follows:

$$\frac{dV_{\text{cell}}}{dQ_{\text{cell}}} = \frac{1}{s_{\text{pos}}} \frac{dV_{\text{pos}}(s_{\text{pos}}q_{\text{pos}} + \delta_{\text{pos}})}{dq_{\text{pos}}} - \frac{1}{s_{\text{neg}}} \frac{dV_{\text{neg}}(s_{\text{neg}}q_{\text{neg}} + \delta_{\text{neg}})}{dq_{\text{neg}}} \quad (10)$$

However, even if the approach in this study is to fit dV/dQ-peaks, Honkura et al. have showed that it also is possible to fit data from electrode material with no obvious dV/dQ-peaks using this method [44].

Fitting of half cell data to full cell data was performed by using a graphical user interface program developed in MatLab®. Since the negative electrode consists of  $\text{Li}_4\text{Ti}_5\text{O}_{12}$ , the dV/dQ plot is flat over almost the whole capacity range, as showed in Fig. 1d, meaning that the two visible dV/dQ-peaks in the full cell plot solely relates to the positive electrode. Hence, dV/dQ fitting of the positive electrode to the corresponding full cell was in this case done solely by scaling ( $s_{\text{pos}}$ ) and shifting ( $\delta_{\text{pos}}$ ) the positive electrode half cell data, according to Equation (11).

$$\frac{dV_{\text{cell}}}{dQ_{\text{cell}}} = \frac{1}{s_{\text{pos}}} \frac{dV_{\text{pos}}(s_{\text{pos}}q_{\text{pos}} + \delta_{\text{pos}})}{dq_{\text{pos}}} \quad (11)$$

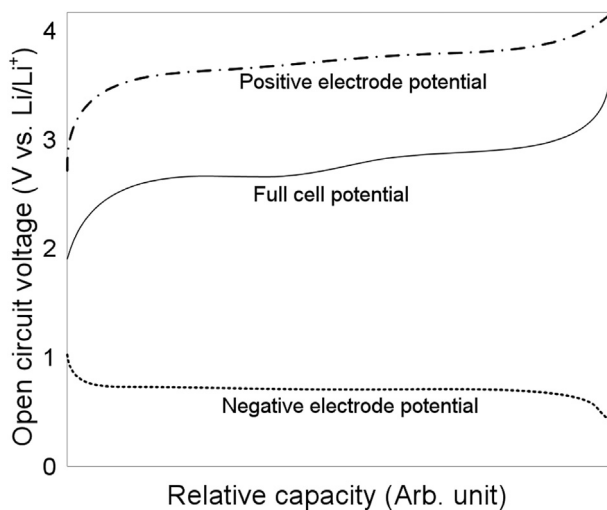


**Fig. 9.** Schematic overview over potential vs. capacity for a perfectly matched cell including corresponding positive and negative electrode capacities.



The results are presented in Fig. 10a and b that show fitted and measured OCV curves for the calendar-aged and the cycle-aged cell respectively, including corresponding fitted positive and negative half cell data. The two distinctive peaks that appear when differentiating the full cell and positive electrode OCV data were used in the fitting process. The half cell peak height and distance between peaks were fitted to the full cell by adjusting  $s_{\text{pos}}$  and the x-axis peak positions were fitted to the full cell by adjusting the slippage  $\delta_{\text{pos}}$  (Fig. 10c). The negative scaling factor  $s_{\text{neg}}$  was assumed equal to the positive since the same size of electrode samples were used in the half cells and since it was seen during disassembly of the cells that the area of the electrodes was the same. Finally, the negative electrode slippage  $\delta_{\text{neg}}$  was derived by using Equation (7) together with the already calculated parameters.

The error between the fitted and the measured voltage profiles for the calendar-aged cell (Fig. 10a) is within  $\pm 5$  mV between  $\sim 530$  mAh and  $\sim 3590$  mAh, corresponding to an SOC-window of  $\sim 15\%$  to  $\sim 98\%$ . Outside this window the error is higher, probably due to higher impedance but still within  $\pm 10$  mV for almost the complete SOC-region. The fitting parameters for the calendar-aged cell were calculated to  $s_{\text{pos}} = s_{\text{neg}} = 707$ ,  $\delta_{\text{pos}} = -18$  mAh and  $\delta_{\text{neg}} = -177$  mAh. For the cycle-aged cell in Fig. 10b the voltage error is comparable to the result of the calendar-aged cell; the error is less than  $\pm 5$  mV between  $\sim 255$  mAh and  $\sim 2612$  mAh, corresponding to an SOC-window of  $\sim 10\%$  to  $\sim 99\%$ . However, outside this window the difference is a larger for the cycle-aged cell than the calendar-aged cell. The fitting parameters for the cycle-aged cell were calculated to  $s_{\text{pos}} = s_{\text{neg}} = 634$ ,  $\delta_{\text{pos}} = -8.4$  mAh and  $\delta_{\text{neg}} = -729$  mAh.

From this analysis it is discovered that this cell is limited by the positive electrode at completely discharged state and by the negative electrode at completely charged state for both the cycle-aged and the calendar-aged cell, even though the positive electrode has lower capacity than the negative electrode for the cycle-aged cell and vice versa for the calendar-aged cell. There is only a

small difference between the slippage of the calendar-aged positive electrode and the cycle-aged positive electrode. The slippage for the cycle-aged negative electrode is however significantly larger than the calendar-aged negative electrode slippage and is due to loss of positive electrode active material. From Fig. 10a it is possible to see that this cell is unbalanced already in its pristine condition. Although there is an excess of positive electrode active material in the calendar-aged cell, the full capacity of the negative electrode active material is not used, corresponding to the  $-177$  mAh slip. For the cycle-aged cell it is seen that the positive electrode capacity has diminished and that the negative electrode capacity, that has only slightly been reduced, has slipped considerably to the left (Fig. 10b). Due to this behavior, the positive electrode capacity is not fully utilized and the cell capacity is hence smaller than the limiting electrode capacity in this case as well. This behavior is the opposite to similar work on cells with  $\text{LiFePO}_4$  positive electrode and graphite negative electrode, where the negative electrode contributes to the largest part of the loss of cell capacity [45].

### 3.7. State of charge operating window

The large slippage of the negative electrode curve for the cycle-aged cell in Fig. 10b is probably mainly correlated to loss of positive electrode active material. This statement can also be visualized by a graphical representation of the relationship between the electrodes in a so called SOC operating window. The theory behind this graphical representation has previously been published in literature [46,47]. The x-axis in Fig. 11 represents the  $\text{Li}^+$ -content or SOC for the negative electrode and the y-axis represents the  $\text{Li}^+$ -content or SOC for the positive electrode. The diagonal solid line represents an ideally matched cell, corresponding to the schematic voltage vs. capacity plot in Fig. 9. Fig. 11a shows two charge/discharge paths (dashed lines) in a SOC operating window. Path (i) describes an initial path represented by data

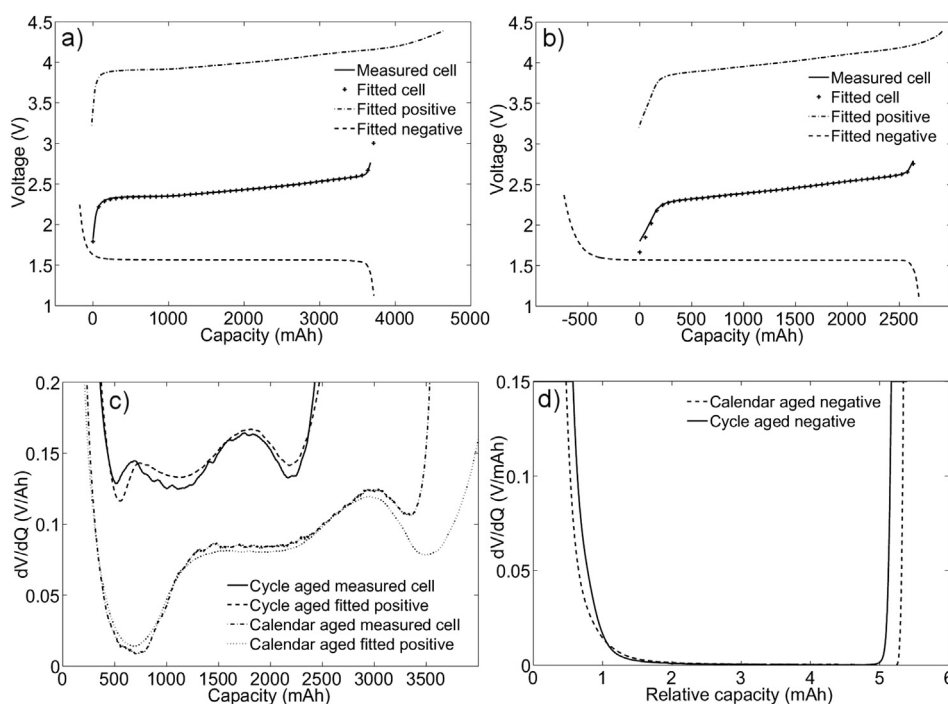


**Fig. 10.** (a) Measured and calculated calendar-aged capacity as well as fitted half cell capacities, (b) measured and calculated cycle-aged capacity as well as fitted half cell capacities, (c) full cell  $dV/dQ$  plots and fitted positive electrode  $dV/dQ$  plots, (d)  $dV/dQ$  plots for the negative electrode.



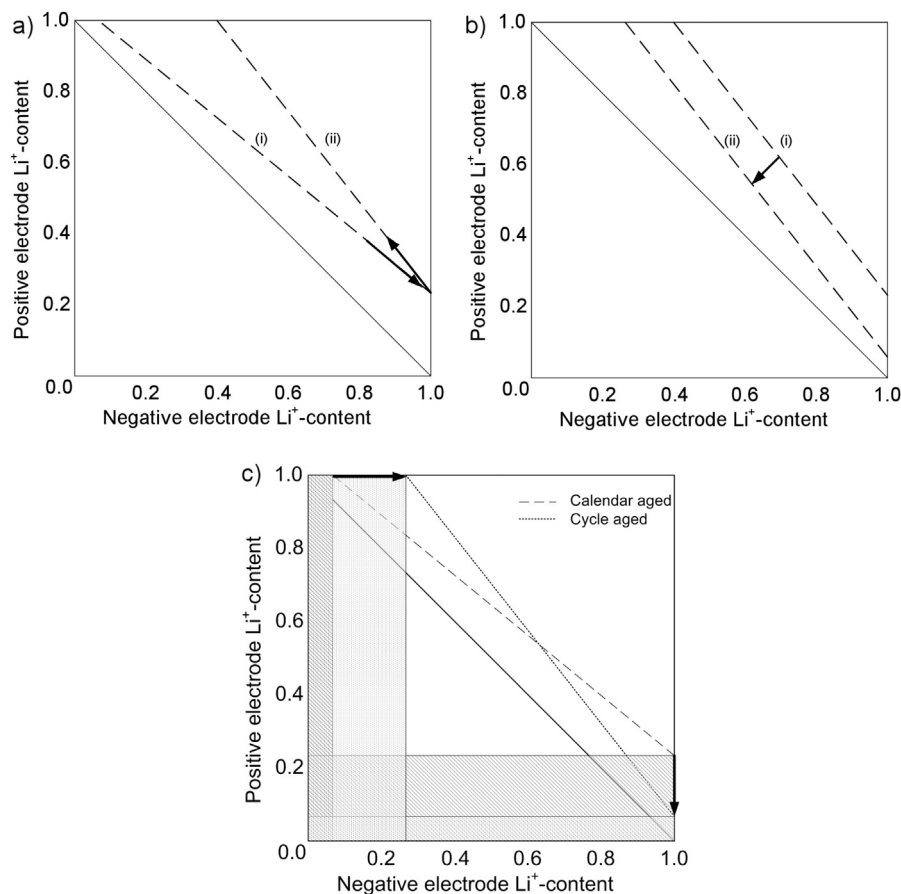


**Fig. 11.** (a) Schematic SOC operating window describing loss of positive active material in a charged state going from the original state (i) to the new state (ii), (b) Schematic SOC operating window describing loss of cyclable lithium going from the original state (i) to the new state (ii), (c) SOC operating window for the cycle-aged and calendar-aged cell calculated from half cell data. The solid diagonal line represents a perfectly matched cell. The solid grayed areas represent unused positive and negative electrode active material for the cycle-aged cell. The lined grayed areas represent unused positive and negative electrode active material for the calendar-aged cell.

from the calendar-aged cell. Path (ii) describes a path where positive electrode active material is lost at the charged state without cyclable lithium being part of the process. In this the positive electrode will have a lithiation degree of  $\sim 0.22$  when the negative electrode is fully lithiated (1.0) as for path (i), but the slope of the line representing the relationship between the electrodes will be different. The slope is changed since the positive electrode SOC now corresponds to a smaller negative electrode SOC-window, i.e. the ratio between positive active material and negative active material is smaller. If also cyclable lithium is lost in a discharged state at the positive electrode, lithium will be removed from the positive electrode resulting in a lowered positive electrode SOC-state. Since the ratio between positive active material and negative active material is constant in this case, the slope of the new path in the SOC operating window will stay the same. This results in a displacement of the path to the left in the SOC operating window, displayed as the shift from path (i) to path (ii) in Fig. 11b. It can be noticed that loss of cyclable lithium in this particular case actually increases cell capacity, i.e. the slippage of the negative electrode curve in Fig. 10b is reduced when cyclable lithium is lost, and hence more of the surplus positive electrode capacity is used. The loss of cyclable lithium could relate to film formation taking place on the negative electrode. Fig. 11c shows the SOC operating window for both the cycled- and the calendar-aged cell where the calendar-aged path corresponds to path (i) in Fig. 11a and the cycle-aged path

corresponds to path (ii) in Fig. 11b. The dashed areas represent unused positive and negative electrode active material for the calendar-aged cell while the dotted grayed areas represents unused positive and negative electrode active material for the calendar-aged cell.

It is seen that the calendar-aged cell has an excess of positive electrode active material represented by a larger vertical dashed area than the horizontal dashed area, which is one direct consequence of a shallower slope of the dashed line compared to the solid line. For the cycle-aged cell the situation is reversed in the sense that the vertical dotted area is smaller than the horizontal due to a steeper slope of the dotted line, corresponding to an excess of negative electrode active material. The utilization of the positive electrode has increased while the utilization of the negative electrode has decreased which is visualized in Fig. 11c by the vertical and horizontal arrows respectively. Both the dashed and the dotted lines are positioned above the solid line in Fig. 11 which indicates that there is an excess of cyclable lithium in both cases [46]. This is not surprising since only minor formation of lithium consuming surface films is expected in this type of battery cells. From this SOC operating window it is also easy to see that the positive electrode is limiting the full cell capacity in the fully discharged state (positive electrode  $\text{Li}^+$ -content equals 1.0), and that the negative electrode is limiting the full cell capacity in the fully charged state (negative electrode  $\text{Li}^+$ -content equals 1.0) both for the calendar-aged cell and the cycle-aged cell.



#### 4. Conclusions

A study on aging mechanisms of commercial composite metal oxide/Li<sub>4</sub>Ti<sub>5</sub>O<sub>12</sub> battery cells was done. The study shows the possibility to perform advanced electrochemical analysis on lithium-ion cells and corresponding half cells using standard battery cycling equipment. The results show that the negative electrode consisting of Li<sub>4</sub>Ti<sub>5</sub>O<sub>12</sub> has a relatively small loss of active material when cycled at an elevated temperature. This small loss of active material could origin from interaction between of Li<sub>4</sub>Ti<sub>5</sub>O<sub>12</sub> and the manganese found throughout the negative electrode material. The positive electrode material consisting of a combination of LiMn<sub>2</sub>O<sub>4</sub> and LiCoO<sub>2</sub> showed a significant capacity fade when cycled at an elevated temperature. It was showed that both the LiMn<sub>2</sub>O<sub>4</sub> phase and the LiCoO<sub>2</sub> phase had been influenced by the cycling. The capacity fade is suggested to relate to Mn<sup>2+</sup> dissolution, and possibly also to transformation of LiCoO<sub>2</sub> into other phases, for example the cubic spinel phase, Li<sub>2</sub>Co<sub>2</sub>O<sub>4</sub>. The large impedance rise could relate to changes in both the LiMn<sub>2</sub>O<sub>4</sub> phase and the LiCoO<sub>2</sub> phase. Loss of cyclable lithium was also detected for the cycle-aged cell, possible connected to surface film formation on the negative electrode with following gas generation due to consumption of electrolyte solvent. The initial surplus of positive material is not fully utilized even after cycling due to the excess of cyclable lithium still present at the end of test. The capacity of this cell type is limited by the negative electrode when fully charged and by the positive electrode when fully discharged, both when it is fresh and when it has been aged. The tested cell type shows excellent calendar aging qualities with both stable capacity and impedance over time. However, calendar aging seems to be affected by the cycling history of the cell. By combining several test methods and using half cells from harvested electrode material it was possible to obtain a deeper knowledge of the aging behavior of this type of commercial lithium ion battery cell.

#### Acknowledgments

This work was funded by Scania CV AB and the Swedish Energy Agency. Carl Tengstedt is acknowledged for the assistance with the SEM work and Jens Groot for helping with MatLab questions and fruitful discussions.

#### References

- [1] I. Bloom, A.N. Jansen, D.P. Abraham, J. Knuth, S.A. Jones, V.S. Battaglia, G.L. Henriksen, *J. Power Sources* 139 (2005) 295–303.
- [2] I. Bloom, J. Christophersen, K. Gering, *J. Power Sources* 139 (2005) 304–313.
- [3] I. Bloom, J.P. Christophersen, D.P. Abraham, K.L. Gering, *J. Power Sources* 157 (2006) 537–542.
- [4] A.J. Smith, H.M. Dahn, J.C. Burns, J.R. Dahn, *J. Electrochem. Soc.* 159 (2012) A705–A710.
- [5] A.J. Smith, J.C. Burns, J.R. Dahn, *Electrochem. Solid State Lett.* 14 (2011) A39–A41.
- [6] Ralph J. Brodd (Ed.), *Batteries for Sustainability: Selected Entries from the Encyclopedia of Sustainability Science and Technology*, Springer Science and Media+Business Media, New York, 2013.
- [7] T. Ohzuku, A. Ueda, N. Yamamoto, *J. Electrochem. Soc.* 142 (1995) 1431–1435.
- [8] Denso (Ed.), 2012, <http://www.globaldenso.com/en/newsreleases/121004-01.html>.
- [9] Toshiba (Ed.), 2012, [http://www.toshiba.co.jp/about/press/2012\\_09/pr0601.htm](http://www.toshiba.co.jp/about/press/2012_09/pr0601.htm).
- [10] T. Yuan, X. Yu, R. Cai, Y. Zhou, Z. Shao, *J. Power Sources* 195 (2010) 4997–5004.
- [11] D. Wu, *Ionics* 18 (2012) 559–564.
- [12] P. Svens, J. Lindström, O. Gelin, M. Behm, G. Lindbergh, *Energies* 4 (2011) 741–757.
- [13] P.I. Svens, J. Lindström, M. Behm, G. Lindbergh, *ECS Trans.* 41 (2012) 13–26.
- [14] J. Rodriguezcarvajal, *Phys. B* 192 (1993) 55–69.
- [15] H. Berg, J.O. Thomas, *Solid State Ionics* 126 (1999) 227–234.
- [16] R.J. Gummow, D.C. Liles, M.M. Thackeray, *Mater. Res. Bull.* 28 (1993) 235–246.
- [17] D. Zhang, B.S. Haran, A. Durairajan, R.E. White, Y. Podrazhansky, B.N. Popov, *J. Power Sources* 91 (2000) 122–129.
- [18] J. Li, E. Murphy, J. Winnick, P.A. Kohl, *J. Power Sources* 102 (2001) 294–301.
- [19] S. Brown, K. Ogawa, Y. Kumeuchi, S. Enomoto, M. Uno, H. Saito, Y. Sone, D. Abraham, G. Lindbergh, *J. Power Sources* 185 (2008) 1454–1464.
- [20] S.-C. Park, Y.-M. Kim, Y.-M. Kang, K.-T. Kim, P.S. Lee, J.-Y. Lee, *J. Power Sources* 103 (2001) 86–92.
- [21] N.V. Kosova, E.T. Devyatkina, V.V. Kaichev, A.B. Slobodyuk, *Solid State Ionics* 192 (2011) 284–288.
- [22] G.G. Amatucci, J.M. Tarascon, L.C. Klein, *J. Electrochem. Soc.* 143 (1996) 1114–1123.
- [23] H. Berg, H. Rundlov, J.O. Thomas, *Solid State Ionics* 144 (2001) 65–69.
- [24] A.J. Smith, J.C. Burns, D. Xiong, J.R. Dahn, *J. Electrochem. Soc.* 158 (2011) A1136–A1142.
- [25] M. Dubarry, B.Y. Liaw, M.-S. Chen, S.-S. Chyan, K.-C. Han, W.-T. Sie, S.-H. Wu, *J. Power Sources* 196 (2011) 3420–3425.
- [26] M. Dubarry, B.Y. Liaw, *J. Power Sources* 194 (2009) 541–549.
- [27] C. Weng, Y. Cui, J. Sun, H. Peng, *J. Power Sources* 235 (2013) 36–44.
- [28] J. Groot, in: *Institutionen För Energi Och Miljö, Elteknik, Chalmers Tekniska Högskola*, 2012, p. 146.
- [29] D. Linden, T.B. Reddy, in: *McGraw-Hill*, 2002.
- [30] F.O. Ernst, H.K. Kammiller, A. Roessler, S.E. Pratsinis, W.J. Stark, J. Ufheil, P. Novák, *Mater. Chem. Phys.* 101 (2007) 372–378.
- [31] W. Liu, G.C. Farrington, F. Chaput, B. Dunn, *J. Electrochem. Soc.* 143 (1996) 879–884.
- [32] D. Liu, Z. He, X. Liu, *Mater. Lett.* 61 (2007) 4703–4706.
- [33] Y. Xia, M. Yoshio, *J. Electrochem. Soc.* 143 (1996) 825–833.
- [34] M. Dubarry, C. Truchot, B.Y. Liaw, *J. Power Sources* 219 (2012) 204–216.
- [35] N.V. Kosova, E.T. Devyatkina, V.V. Kaichev, *Russ. J. Electrochem.* 45 (2009) 277–285.
- [36] H. Gabrisch, Y. Ozawa, R. Yazami, *Electrochim. Acta* 52 (2006) 1499–1506.
- [37] H. Gabrisch, R. Yazami, B. Fultz, *J. Power Sources* 119 (2003) 674–679.
- [38] H. Gabrisch, R. Yazami, B. Fultz, *J. Electrochem. Soc.* 151 (2004) A891–A897.
- [39] A. Du Pasquier, A. Blyr, P. Courjal, D. Larcher, G. Amatucci, B. Gérard, J.M. Tarascon, *J. Electrochem. Soc.* 146 (1999) 428–436.
- [40] A. du Pasquier, A. Blyr, A. Cressent, C. Lenain, G. Amatucci, J.M. Tarascon, *J. Power Sources* 81–82 (1999) 54–59.
- [41] H. Kobayashi, H. Sakaebe, K. Komoto, H. Kageyama, M. Tabuchi, K. Tatsumi, T. Kohigashi, M. Yonemura, R. Kanno, T. Kamiyama, *Solid State Ionics* 156 (2003) 309–318.
- [42] Y.-B. He, B. Li, M. Liu, C. Zhang, W. Lv, C. Yang, J. Li, H. Du, B. Zhang, Q.-H. Yang, J.-K. Kim, F. Kang, *Sci. Rep.* 2 (2012) 913.
- [43] M. Dubarry, V. Svoboda, R. Hwu, B.Y. Liaw, *Electrochem. Solid State Lett.* 9 (2006) A454–A457.
- [44] K. Honkura, H. Honbo, Y. Koishikawa, T. Horiba, *ECS Trans.* 13 (2008) 61–73.
- [45] M. Klett, R. Eriksson, J. Groot, P. Svens, K. Ciosek Högstöm, R.W. Lindström, H. Berg, T. Gustafson, G. Lindbergh, K. Edström, *J. Power Sources* 257 (2014) 126–137.
- [46] J. Christensen, J. Newman, *J. Electrochem. Soc.* 152 (2005) A818–A829.
- [47] J. Christensen, J. Newman, *J. Electrochem. Soc.* 150 (2003) A1416–A1420.